

Synthesis of Ultrawide Band Gap TeO₂ Nanoparticles by Pulsed Laser Ablation in Liquids: Top Ablation versus Bottom Ablation

Rajendra Subedi and Grégory Guisbiers*

Cite This: *ACS Omega* 2024, 9, 25832–25840

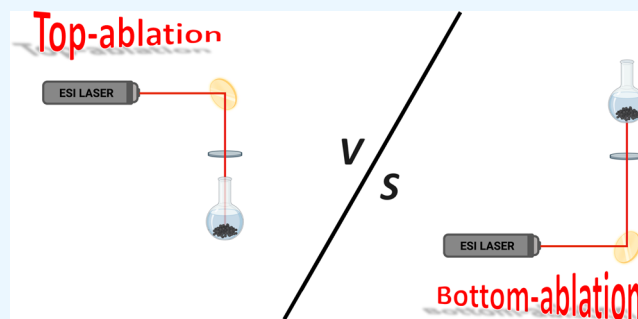
Read Online

ACCESS |

Metrics & More

Article Recommendations

ABSTRACT: Ultrawide band gap (UWBG) semiconductors are the future components of electronic devices due to their large energy band gap (>3.2 eV). In this article, spherical TeO₂ nanoparticles, with sizes around $\sim 39 \pm 12$ and $\sim 29 \pm 6$ nm, were successfully synthesized by irradiating a pure tellurium target, totally submerged in ethanol, using a “Top-ablation” or “Bottom-ablation” synthesis protocol, respectively. Mostly, α -TeO₂ nanoparticles were created (>95%) with only a small amount of γ -TeO₂ nanoparticles being produced (<5%). Both colloids exhibited a ζ -potential larger than |30 mV|, indicating a stable colloidal solution. The energy band gaps of the TeO₂ nanoparticles synthesized by the Top-ablation and Bottom-ablation synthesis protocols were determined to be around 5.3 and 5.8 eV, respectively. Finally, TeO₂ UWBG nanoparticles were successfully synthesized using either a Top-ablation or Bottom-ablation synthesis protocol. The main advantage of the Bottom-ablation synthesis protocol is its ability to obtain smaller nanoparticles compared to that of the Top-ablation synthesis protocol.



1. INTRODUCTION

Since the invention of the transistor at Bell Laboratories in 1947, the scientific community has witnessed the spread of semiconductors in our daily life. However, semiconductor-based devices are currently approaching their limits of performance. Consequently, ultrawide band gap (UWBG) semiconductors (i.e., a semiconductor with its energy band gap larger than 3.2 eV—largest value for a visible radiation¹), such as aluminum nitride (AlN),² gallium nitride (GaN),³ aluminum gallium nitride (AlGaN),³ gallium oxide (Ga₂O₃),⁴ boron nitride (BN),⁵ silicon carbide (SiC),⁶ diamond (C),⁷ and tellurium dioxide (TeO₂),⁸ are being investigated to develop the next generation of electronic devices. Indeed, an increase in the energy band gap leads to a higher electric field breakdown suitable for extreme miniaturization. Consequently, UWBG semiconductors allow electronic devices to operate in harsh environmental conditions such as high temperatures and high radiation levels.^{3,9}

Tellurium dioxide (TeO₂) is an important UWBG binary compound made of tellurium (Te) and oxygen (O) atoms, both belonging to column VI of the periodic table (known as the chalcogenide elements). This unique combination of two different chalcogenide elements within the same crystalline structure produces lone pair electrons, which is responsible for the remarkable physical properties of TeO₂.¹⁰ Indeed, TeO₂ is a dielectric,¹¹ piezoelectric,¹² and opto-acoustic¹³ material which is of great interest for fundamental science and technology.

Moreover, TeO₂ exhibits three different polymorphs: α -TeO₂ (paratellurite, a tetragonal structure with four TeO₂ units per unit cell), β -TeO₂ (tellurite, an orthorhombic structure with eight TeO₂ units per unit cell), and γ -TeO₂ (an orthorhombic structure with four TeO₂ units per unit cell).^{11,14–16} Among all of the three polymorphs, α -TeO₂ is the most thermodynamically stable.¹⁷ At the bulk scale, α -TeO₂ has a direct band gap of ~ 3.50 eV and an indirect band gap of ~ 2.89 eV;^{18,19} β -TeO₂ has a direct band gap of ~ 2.26 eV,^{11,18} and γ -TeO₂ exhibits an indirect band gap of ~ 3.41 eV.^{11,20,21} Therefore, among all of the TeO₂ polymorphs, the α -phase exhibits the largest energy band gap, while the β -phase exhibits the smallest.

Currently, there is strong motivation within the scientific community to develop TeO₂ nanostructures. So far, they have been produced by different methods such as spray analysis,²² sonochemistry,²³ hydrothermal,^{24,25} evaporation,²⁶ biosynthesis,²⁷ wet chemistry,²⁸ and pulsed laser ablation in liquids (PLAL, Table 1).^{29–34} PLAL offers several advantages in comparison to other synthesis techniques. First, PLAL does

Received: January 4, 2024

Revised: May 22, 2024

Accepted: May 27, 2024

Published: June 5, 2024

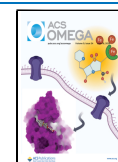


Table 1. TeO₂ Nanoparticles Synthesized by PLAL

authors	year	laser	wavelength (nm)	repetition rate (Hz)	time (s)	solvent	results	setup
Khalef ²⁹	2014	Nd:YAG	1064	1	20	DI water	TeO ₂ NPs	top ablation
Liu et al. ³⁴	2016	Nd:YAG	1064	20	2	DI water	TeO ₂ & Te NPs	top ablation
					10	methanol		
					180	ethanol		
						acetone		
						dichloro		
						methane		
Guisbiers et al. ³³	2017	Nd:YAG	1064	20	900	DI water	TeO ₂ & Te NPs	top ablation
						acetone		
Saraeva et al. ³¹	2020	Yb-doped	1040	20,000	?	DI water	TeO ₂ NPs	top ablation
Khalef et al. ³²	2021	Nd:YAG	1064	1	50	DI water	TeO ₂ NPs	top ablation
Hesabizadeh et al. ³⁰	2022	Nd:YAG	1064	1000	300	DI water	TeO ₂ NPs	top ablation
this work	2024	Nd:YAG	1064	1000	300	ethanol	TeO ₂ NPs	top ablation & bottom ablation

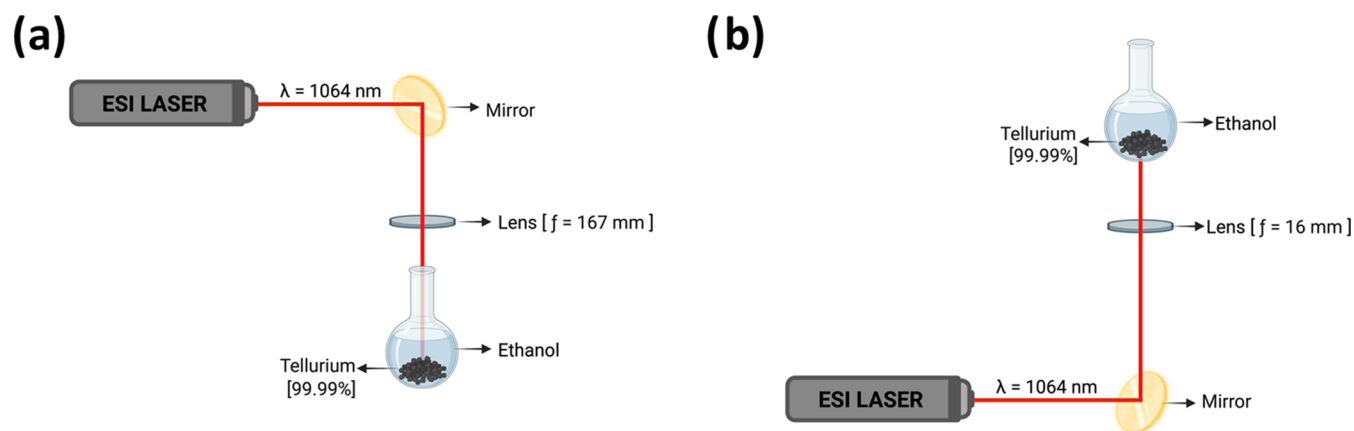


Figure 1. Sketch showing the (a) Top-ablation and (b) Bottom-ablation PLAL synthesis protocols.

not require capping ligands as wet chemistry does.^{35–38} Specifically, PLAL produces nanoparticles with clean surfaces because it relies on electrostatic repulsion instead of steric repulsion. Second, PLAL can produce phases that are hardly achievable by wet chemistry. In this study, α -TeO₂ and γ -TeO₂ nanoparticles have been produced by PLAL using “Top-ablation” and “Bottom-ablation” synthesis protocols. Both protocols were compared. Indeed, the size, shape, chemical composition, and optical properties of TeO₂ nanoparticles were determined for each synthesis protocol.

2. MATERIALS AND METHODS

2.1. PLAL Synthesis. A Q-switched Nd:YAG laser from Electro Scientific Industries operating at 1064 nm was used to irradiate the target, made of two layers of bulk Te pellets (99.99% from Sigma-Aldrich 263303-25G), each pellet with a diameter of \sim 2 mm; consequently, the overall thickness of the target was \sim 4 mm. Te pellets were rinsed with ethanol and then immersed in 5 mL of ethanol, contained in a 50 mL round single-neck glass flask. If the laser beam hits the Te pellets from above, it is called a Top-ablation synthesis protocol (Figure 1a), while if it hits the Te pellets from underneath the container, it is called a Bottom-ablation synthesis protocol (Figure 1b). The infrared laser beam ($\lambda = 1064$ nm) was reflected onto a flat mirror, inclined at 45° with respect to the laser rail. After being reflected, the laser beam was focused by a biconvex lens of focal length 167 or 16 mm onto the Te pellets. The choice of the focal length depends on

the synthesis protocol, 167 mm for the Top-ablation synthesis protocol and 16 mm for the Bottom-ablation synthesis protocol. The power of the laser beam was measured at around \sim 11.2 W with an energy per pulse of \sim 11.2 mJ as the repetition rate of the laser was fixed at 1 kHz. The laser fluence was determined to be \sim 118 and \sim 178 J/cm² for the Top-ablation and Bottom-ablation synthesis protocols, respectively. Finally, the target was irradiated for 5 min.

2.2. Physicochemical Characterization. After the synthesis, the target made of Te pellets was removed from the flask and the colloid was poured into a 5 mL opaque plastic microtube for sample preservation. Then, dynamic light scattering (DLS, NanoBrook 90Plus from Brookhaven Instruments Corporation) was performed to determine the diameter and stability of TeO₂ nanoparticles. A pH meter from Thermo Scientific (Orion star A211 pH) was used to determine the pH value of each colloid. Before any measurements, the pH meter was calibrated using three different standard solutions with pH values set at 4, 7, and 10. Scanning electron microscopy (SEM, JEOL JSM-7000F, operating at 15 kV and equipped with an energy-dispersive X-ray, EDX, spectrometer) was used to capture the images of nanoparticles and identify their internal chemical composition. Their diameter was analyzed by using ImageJ software. To prepare the sample for SEM, a droplet of the colloid was dropped onto a silicon wafer and dried in a glovebox. The chemical composition and crystalline phase of the nanoparticles were identified by Raman spectroscopy (EZRaman-N from Enwave Optronics, Inc.), X-ray diffraction

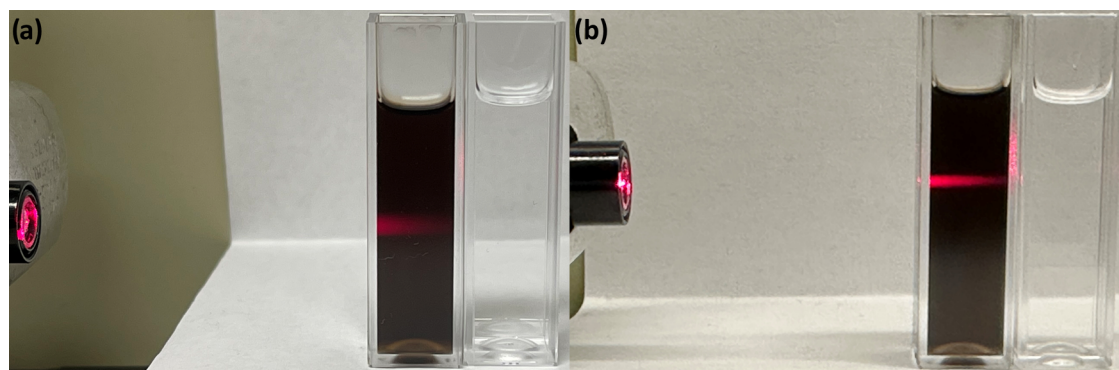


Figure 2. Tyndall effect observed in the colloid synthesized by a (a) Top-ablation PLAL synthesis protocol@1 kHz and (b) Bottom-ablation PLAL synthesis protocol@1 kHz. The left cuvette contains TeO₂ NPs synthesized by PLAL, while the right cuvette contains only the ethanol solvent, for reference purposes only.

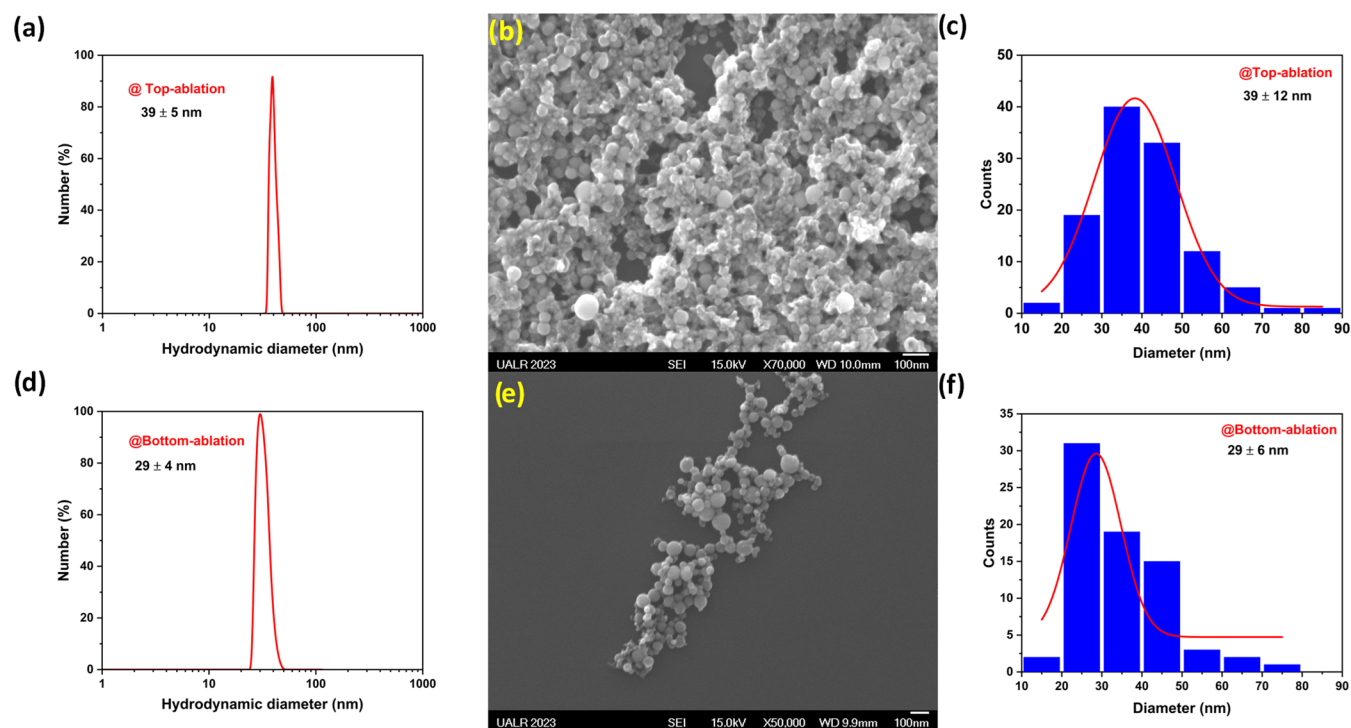


Figure 3. Size distribution and morphology. (a) Size distribution of TeO₂ NPs, synthesized by a Top-ablation PLAL synthesis protocol at 1 kHz, was determined by dynamic light scattering. (b) SEM image of TeO₂ NPs synthesized by a Top-ablation PLAL synthesis protocol at 1 kHz. (c) Size distribution analysis performed by ImageJ of the NPs corresponding to the SEM image shown in (b). (d) Size distribution of TeO₂ NPs, synthesized by a Bottom-ablation PLAL synthesis protocol at 1 kHz, determined by dynamic light scattering. (e) SEM image of TeO₂ NPs synthesized by a Bottom-ablation PLAL synthesis protocol at 1 kHz. (f) Size distribution analysis performed by ImageJ of the NPs corresponding to the SEM image shown in (e).

(XRD, Miniflex 600 from Rigaku), and transmission electron microscopy (TEM, JEOL 2100F, operating at 200 kV). For Raman spectroscopy and X-ray diffraction, the colloid was centrifuged at 13,000 rpm for 30 min using a Sorvall Legend Micro 17 from Thermo Fisher Scientific. The sedimented particles were recovered and dried in a glovebox before their Raman and XRD analyses. Finally, optical characterization was performed by using a UV–visible spectrometer (Cary 60 from Agilent).

3. RESULTS AND DISCUSSION

Colloids produced by both PLAL protocols are shown in Figure 2. Both colloids exhibited a dark gray color, characteristic of TeO₂ nanoparticles being produced, as already

observed by Khalef²⁹ and Hesabizadeh et al.³⁰ By shining a red laser pointer through the colloid, the red laser light ($\lambda = 650$ nm) is being scattered, indicating the presence of particles within the sample. This phenomenon is known as the Tyndall effect.³⁹

The size distribution and morphology of the particles were determined by DLS and SEM as shown in Figure 3. It can be seen in Figure 3a that the size distribution of the particles was centered at around 39 ± 5 nm. The shape of the nanoparticles was spherical, as observed on the SEM image (Figure 3b). Moreover, the size of the nanoparticles was statistically measured by using ImageJ software, indicating an average size at around 39 ± 12 nm (Figure 3c), which confirms the results obtained from DLS. Similarly, for the Bottom-ablation

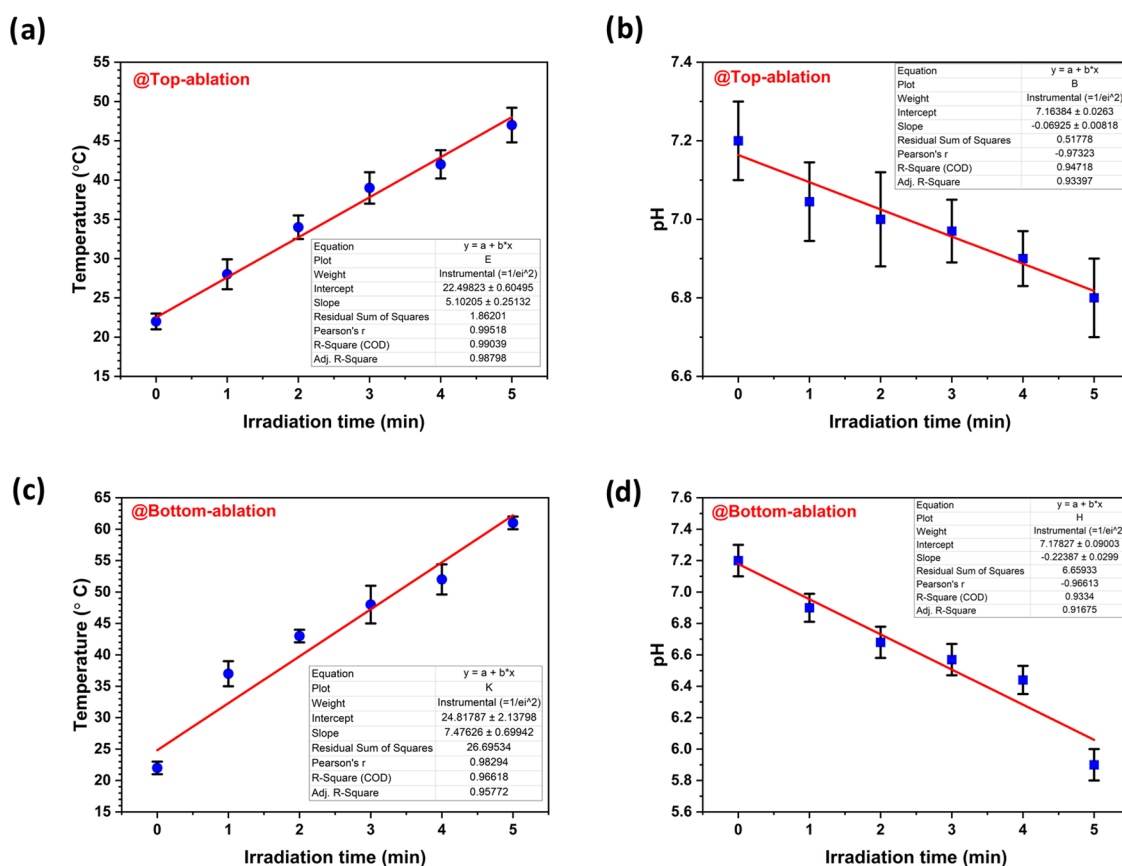


Figure 4. Evolution of the temperature and pH of the colloid during Top ablation and Bottom ablation. (a) Temperature versus irradiation time and (b) pH versus irradiation time for a Top-ablation synthesis protocol. (c) Temperature versus irradiation time and (d) pH versus irradiation time for a Bottom-ablation synthesis protocol.

synthesis protocol, the size distribution and morphology of the particles are shown in Figure 3d–f. It can be seen that the size distribution of the particles was centered at around 29 ± 4 nm (Figure 3d). It is seen from the SEM image (Figure 3e) that the particles are spherical in shape. The statistical size measurement from ImageJ software (Figure 3f) shows that the average size of the particles is at around 29 ± 6 nm, which is in very good agreement with the DLS measurement. Therefore, the average size of the particles synthesized by the Bottom-ablation synthesis protocol was smaller than that obtained with the Top-ablation synthesis protocol. This can be explained by three reasons. The first reason is when being irradiated from underneath the container, the plasma plume cannot expand freely like it would in a Top-ablation configuration, consequently, affecting the nucleation and growth of the nanoparticles. The second reason is that the nanoparticles get trapped between the bulk target and the glass container; consequently, particles get photo-fragmented more often by the laser beam, in comparison to the Top-ablation synthesis protocol. The third reason is the thickness of liquid between the container and the target being much smaller than the thickness of liquid above the target in the Top-ablation synthesis protocol, consequently, providing more energy to the target. For information, the laser beam did not penetrate through the pellet, whatever the synthesis protocol used; because the Te pellets were too thick, exhibiting a thickness of around ~ 2 mm. Consequently, only the surface of the pellet was ablated, whatever the synthesis protocol being used.

Before starting the irradiation, the temperature and pH of each colloid were initially determined at $T = 22 \pm 1$ °C and 7.2 ± 0.2 , respectively. Then, the temperature and pH were measured every minute during the entire time period of the synthesis (i.e., 5 min). As shown in Figure 4, the temperature increased during the synthesis while the pH decreased. Higher temperatures were reached for the Bottom ablation than the Top ablation, while lower pH was reached for Bottom ablation compared to Top ablation. Moreover, the ζ -potential of the colloids was measured at around $\zeta = 34 \pm 1$ and $\zeta = 50 \pm 2$ mV, immediately after the synthesis for the Top-ablation and Bottom-ablation synthesis protocols, respectively. By exhibiting such ζ -potential values, the colloids were considered to be stable with time in both cases. Indeed, a colloid exhibiting a ζ -potential value between -30 and $+30$ mV is considered to be unstable. Consequently, TeO₂ nanoparticles synthesized in ethanol were more stable than the ones synthesized previously in 2022 in deionized (DI) water, as the ζ -potential in DI water at that time was measured to be around -8 mV.³⁰ Finally, it is interesting to note that the higher ζ -potential value obtained for the colloid synthesized with the Bottom-ablation synthesis protocol is correlated to a larger pH change and a larger temperature change during the irradiation. In the literature, Ali et al.⁴⁰ also found that the pH of the nanofluids decreases when the temperature increases.

The chemical composition and crystalline structure of TeO₂ NPs were identified by using Raman spectroscopy and X-ray diffraction (XRD) as shown in Figure 5. In Figure 5a, the α -TeO₂ (paratellurite) crystalline structure was identified for the

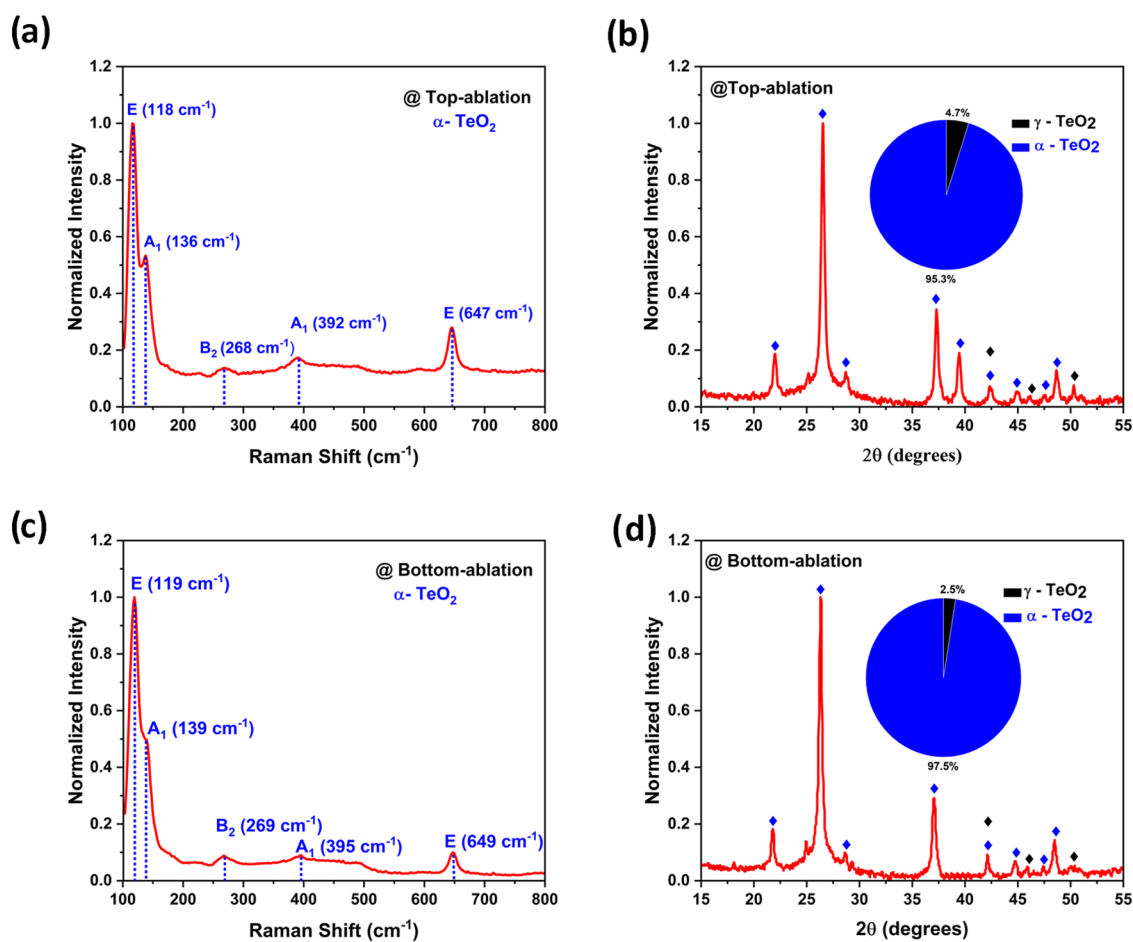


Figure 5. Chemical composition and crystalline phase. (a) Raman spectra revealing the paratellurite tellurium dioxide phase (α -TeO₂) for the Top-ablation PLAL synthesis protocol. The γ -TeO₂ phase was not detected by Raman spectroscopy. (b) XRD spectra showing α -TeO₂ and γ -TeO₂ phases for the Top-ablation PLAL synthesis protocol. (c) Raman spectra revealing the paratellurite tellurium dioxide phase (α -TeO₂) for the Bottom-ablation PLAL synthesis protocol. The γ -TeO₂ phase was not detected by Raman spectroscopy. (d) XRD spectra showing α -TeO₂ and γ -TeO₂ phases for the Bottom-ablation PLAL synthesis protocol. The XRD peak identification was done using the following files: crystallography open database entries 1530871 and JCDPS 11-0693 for the α -TeO₂ phase, and crystallography open database entries 1520934 for the γ -TeO₂ phase.

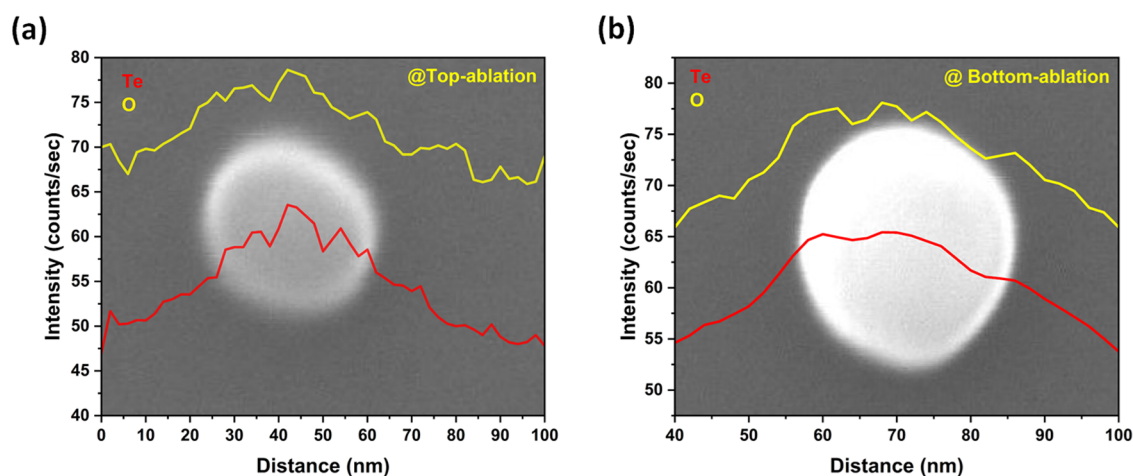


Figure 6. Elemental analysis by SEM. (a) Energy-dispersive X-ray (EDX) line scan through one TeO₂ nanoparticle synthesized by the Top-ablation PLAL synthesis protocol. (b) Energy-dispersive X-ray (EDX) line scan through one TeO₂ nanoparticle synthesized by the Bottom-ablation PLAL synthesis protocol.

nanoparticles synthesized by the Top-ablation protocol. Indeed, the peaks at 118 and 647 cm⁻¹ correspond to the E vibrational mode,³⁴ while those at 136 and 392 cm⁻¹

correspond to the A₁ mode.⁴¹ Similarly, the peak observed at 268 cm⁻¹ represents the B₂ mode.⁴¹ In Figure 5b, the α -TeO₂ (paratellurite) crystalline structure was also confirmed by

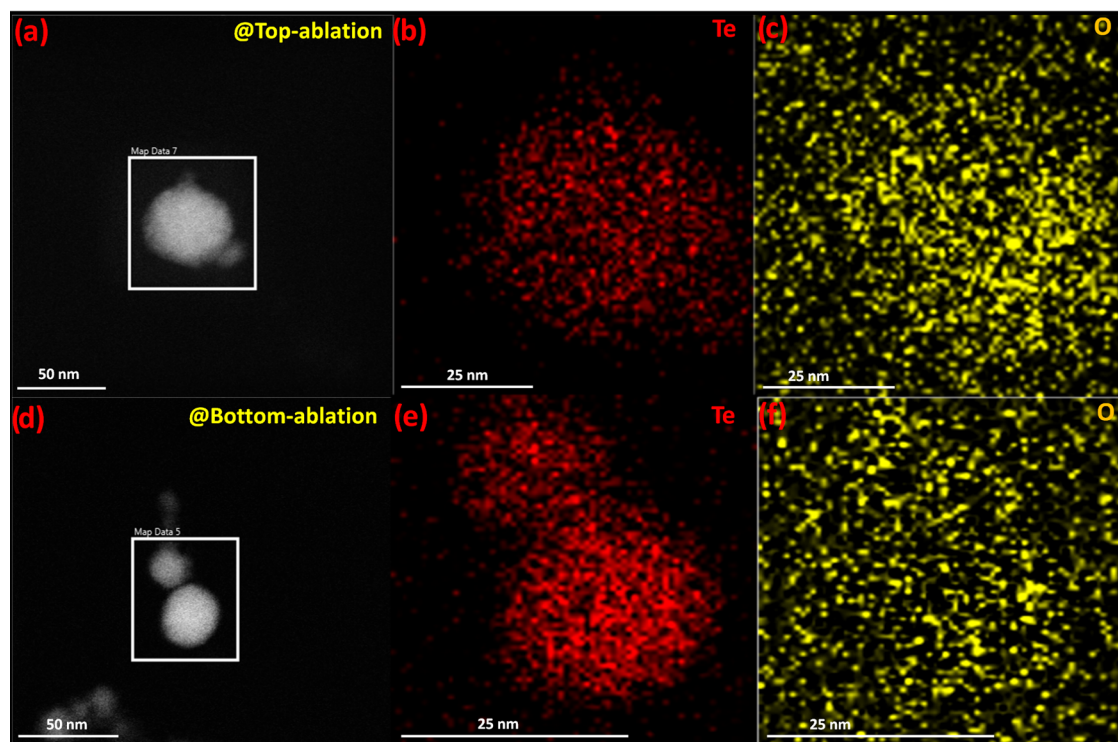


Figure 7. EDX chemical mapping was performed by TEM. (a) TEM image of a TeO₂ nanoparticle synthesized using the Top-ablation PLAL synthesis protocol. (b, c) Corresponding EDX chemical mapping. (d) TEM image of TeO₂ nanoparticles synthesized using the Bottom-ablation PLAL synthesis protocol. (e, f) EDX chemical mapping of the corresponding TEM image of TeO₂ nanoparticles.

XRD, with diffraction peaks located at 21.8° (101), 26.3° (110), 28.6° (111), 37.3° (200), 39.4° (201), 42.3° (210), 44.8° (202), 47.6° (004), and 48.7° (212). However, other peaks were present at 42.3° (201), 46.1° (140), and 50.4° (122), revealing the presence of the γ -TeO₂ phase. By measuring the surface area underneath each XRD peak, it was possible to quantify the proportion of each phase. The colloid synthesized by the Top-ablation synthesis protocol contained 95.3% of the α -TeO₂ phase and 4.7% of the γ -TeO₂ phase. Therefore, α -TeO₂ is the dominant phase compared to the γ -TeO₂ phase. By using the Scherrer equation, the crystallite size was determined to be around 18 ± 2 nm. As the crystallite size is smaller than the physical size of the nanoparticles (~39 nm), it means that the TeO₂ NPs were polycrystalline.

Similarly, for the Bottom-ablation synthesis protocol, the Raman analysis also confirmed the α -TeO₂ (paratellurite) crystalline structure (Figure 5c). The A₁ vibrational modes³⁴ were shown at 119 and 649 cm⁻¹, while the peaks observed at 139 and 395 cm⁻¹ represented the E vibrational mode.³⁴ The peak at 269 cm⁻¹ corresponded to the B₂ mode.⁴¹ In Figure 5d, the XRD spectra confirmed the α -TeO₂ (paratellurite) crystalline structure of the nanoparticles synthesized by the Bottom-ablation synthesis protocol with peaks located at 21.8° (101), 26.3° (110), 28.7° (111), 37.2° (200), 42.2° (210), 44.8° (202), 47.5° (004), and 48.6° (212). However, other peaks were also noticed at 42.2° (201), 45.9° (140), and 50.4° (122) indicating the presence of the γ -TeO₂ phase. Therefore, with this synthesis protocol, the colloid was made of 97.5% α -TeO₂ phase and 2.5% γ -TeO₂ phase. Consequently, the α -TeO₂ phase is also dominating. By using the Scherrer equation, the crystallite size was determined to be around 19 ± 1 nm. As

the crystallite size is smaller than the physical size of the nanoparticles (~29 nm), the TeO₂ NPs were polycrystalline.

Elemental analysis of the nanoparticles was performed by using an energy-dispersive X-ray spectrometer (EDX) available on the SEM. Figure 6a shows the EDX line scan across one of the TeO₂ nanoparticles, synthesized by the Top-ablation synthesis protocol, consequently revealing the presence of Te and O all across the diameter of the nanoparticle. Similarly, an EDX line scan across one of the TeO₂ nanoparticles synthesized by using the Bottom-ablation protocol is shown in Figure 6b, confirming also the presence of Te and O within the nanoparticle.

In addition, EDX chemical mapping was performed by using TEM in order to confirm the presence of Te and O and show their distribution within the nanoparticles. One TeO₂ nanoparticle synthesized by using the Top-ablation synthesis protocol (Figure 7a) was analyzed. The analysis revealed that the nanoparticle contained Te and O within, as shown in Figure 7b,c. Likewise, EDX chemical mapping on two TeO₂ nanoparticles synthesized by using the Bottom-ablation synthesis protocol (Figure 7d) proved that the nanoparticles contained Te and O as shown in Figure 7e,f, respectively. No carbon contamination was observed on the TeO₂ nanoparticles synthesized in ethanol.

In Figure 8a, the UV–visible spectra showed that the absorbance of TeO₂ NPs synthesized by the Top-ablation PLAL synthesis protocol was maximal at 234 nm. By using the Tauc plot (Figure 8b), their energy band gap was determined to be around ~5.3 eV. However, in Figure 8c, it can be seen that the absorbance of the TeO₂ NPs synthesized by the Bottom-ablation PLAL synthesis protocol was maximal at 213 nm. By using the Tauc plot methodology, their energy band gap was determined to be around ~5.8 eV (Figure 8d). Both

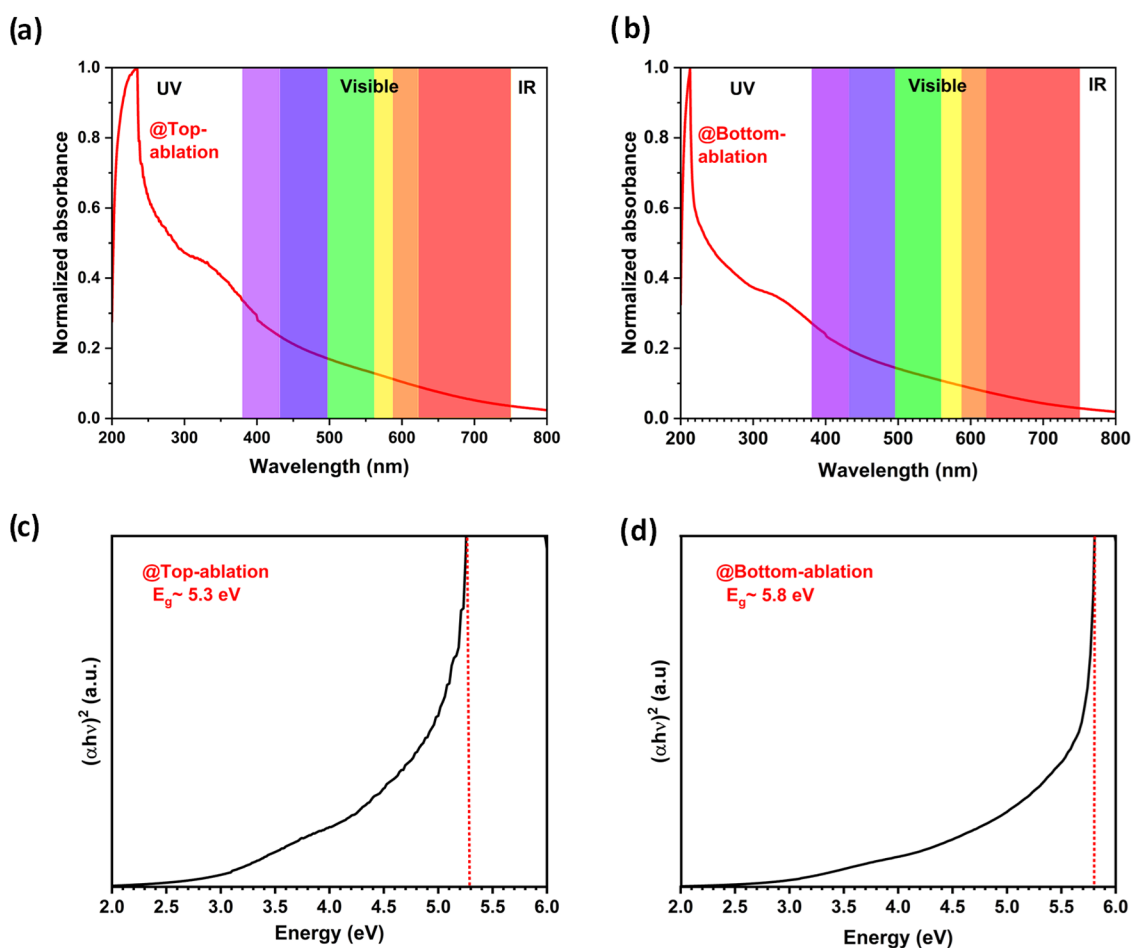


Figure 8. Optical characterization. (a) UV–visible spectra of the colloid synthesized by the Top-ablation PLAL synthesis protocol at 1 kHz. (b) Tauc plot shows an energy band gap of ~ 5.3 eV for the TeO_2 nanoparticles synthesized by the Top-ablation PLAL synthesis protocol. (c) UV–visible spectra of the colloid synthesized by the Bottom-ablation PLAL synthesis protocol at 1 kHz. (d) Tauc plot shows an energy band gap of ~ 5.8 eV for the TeO_2 nanoparticles synthesized by the Bottom-ablation PLAL synthesis protocol.

values of energy band gap are in agreement with the values reported in the literature, Khalef²⁹ and Hesabizadeh et al.³⁰ Theoretically, it is well known that by shrinking the size of a semiconductor, its energy band gap increases.⁴² At the nanoscale, size effects may have two origins: surface effects and quantum effects.⁴³ Here, the increase in the energy band gap observed for both colloids finds its origin in surface effects and not quantum effects. Indeed, to reach the quantum confinement regime with $\alpha\text{-TeO}_2$, it is necessary to shrink the size of the particles below ~ 4 nm. Indeed, the exciton Bohr radius of $\alpha\text{-TeO}_2$ is calculated to be 1.97 nm.⁴⁴ Consequently, the $\alpha\text{-TeO}_2$ nanoparticles, produced by both Top-ablation and Bottom-ablation synthesis protocols, do not qualify to be called “quantum dots”. However, the Bottom-ablation synthesis protocol produces slightly smaller nanoparticles compared to the Top-ablation synthesis protocol. Indeed, larger energy band gaps are measured for TeO_2 nanoparticles synthesized by the Bottom-ablation PLAL synthesis protocol compared to those synthesized by Top-ablation.

4. CONCLUSIONS

In conclusion, we successfully synthesized $\alpha\text{-TeO}_2$ and $\gamma\text{-TeO}_2$ spherical nanoparticles by using Top-ablation and Bottom-ablation PLAL synthesis protocols. But mostly, $\alpha\text{-TeO}_2$ nanoparticles were produced with both protocols (>95%).

Both colloids were stable with time as their ζ -potentials were larger than $|\pm 30$ mV|. Based on the ζ -potential values, it can be concluded that ethanol is a better solvent than deionized water to synthesize TeO_2 nanoparticles by PLAL. Also, the surface of the TeO_2 nanoparticles was kept “naked” without any carbon contamination. The energy band gap of $\alpha\text{-TeO}_2$ nanoparticles was measured at around ~ 5.3 eV for the Top-ablation PLAL synthesis protocol and ~ 5.8 eV for the Bottom-ablation PLAL synthesis protocol; indicating that both protocols are suitable to produce UWBG TeO_2 semiconductors. Finally, it can be concluded that the Bottom-ablation synthesis protocol has two main advantages compared to the Top-ablation synthesis protocol: (1) by producing smaller nanoparticles and (2) by providing a better control on the crystallinity (phase) of the nanoparticles being produced.

■ ASSOCIATED CONTENT

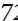
Data Availability Statement

The data underlying this study are available in the published article.

■ AUTHOR INFORMATION

Corresponding Author

Grégory Guisbiers – Department of Physics & Astronomy, University of Arkansas at Little Rock, Little Rock, Arkansas

72204, United States;  orcid.org/0000-0002-4615-6014;
Email: gxguisbiers@ualr.edu, gregory.guisbiers@physics.org

Author

Rajendra Subedi — Department of Physics & Astronomy,
University of Arkansas at Little Rock, Little Rock, Arkansas
72204, United States

Complete contact information is available at:
<https://pubs.acs.org/10.1021/acsomega.3c10497>

Author Contributions

R.S.: Data curation, investigation, formal analysis, visualization, writing—original draft. G.G.: Project administration, funding acquisition, supervision, validation, writing—review and editing.

Notes

Disclaimer Any opinions, findings, and conclusions or recommendations expressed in this material are those of the author(s) and do not necessarily reflect the views of the National Science Foundation.

The authors declare the following competing financial interest(s): G. Guisbiers has patent 63312206 pending.

ACKNOWLEDGMENTS

This material is based on the work supported by the National Science Foundation under Grant No. 2228891. The authors would like to thank Dr. Maria Josefina Arellano-Jimenez (UT Dallas) for performing the TEM analysis and Tina Hesabizadeh (UA Little Rock) for drawing [Figure 1](#).

REFERENCES

- (1) Woods-Robinson, R.; Han, Y.; Zhang, H.; Ablekim, T.; Khan, I.; Persson, K. A.; Zakutayev, A. Wide Band Gap Chalcogenide Semiconductors. *Chem. Rev.* **2020**, *120*, 4007–4055.
- (2) Hickman, A. L.; Chaudhuri, R.; Bader, S. J.; Nomoto, K.; Li, L.; Hwang, J. C. M.; Xing, H. G.; Jena, D. Next generation electronics on the ultrawide-bandgap aluminum nitride platform. *Semicond. Sci. Technol.* **2021**, *36*, No. 044001.
- (3) Higashiwaki, M.; Kaplar, R.; Pernot, J.; Zhao, H. Ultrawide bandgap semiconductors. *Appl. Phys. Lett.* **2021**, *118*, No. 200401.
- (4) Chi, Z.; Asher, J. J.; Jennings, M. R.; Chikoidze, E.; Pérez-Tomás, A. Ga₂O₃ and Related Ultra-Wide Bandgap Power Semiconductor Oxides: New Energy Electronics Solutions for CO₂ Emission Mitigation. *Materials* **2022**, *15*, 1164.
- (5) Laleyan, D. A.; Lee, W.; Zhao, Y.; Wu, Y.; Wang, P.; Song, J.; Kioupakis, E.; Mi, Z. Epitaxial hexagonal boron nitride with high quantum efficiency. *APL Mater.* **2023**, *11*, No. 051103.
- (6) Varley, J. B.; Shen, B.; Higashiwaki, M. Wide bandgap semiconductor materials and devices. *J. Appl. Phys.* **2022**, *131*, No. 230401.
- (7) Yang, J.; Liu, K.; Chen, X.; Shen, D. Recent advances in optoelectronic and microelectronic devices based on ultrawide-bandgap semiconductors. *Prog. Quantum Electron.* **2022**, *83*, No. 100397.
- (8) Guo, S.; Zhu, Z.; Hu, X.; Zhou, W.; Song, X.; Zhang, S.; Zhang, K.; Zeng, H. Ultrathin tellurium dioxide: emerging direct bandgap semiconductor with high-mobility transport anisotropy. *Nanoscale* **2018**, *10*, 8397–8403.
- (9) Wong, M. H.; Bierwagen, O.; Kaplar, R. J.; Umezawa, H. Ultrawide-bandgap semiconductors: An overview. *J. Mater. Res.* **2021**, *36*, 4601–4615.
- (10) Jha, A.; Richards, B. D. O.; Jose, G.; Fernandez, T. T.; Hill, C. J.; Lousteau, J.; Joshi, P. Review on structural, thermal, optical and

spectroscopic properties of tellurium oxide based glasses for fibre optic and waveguide applications. *Int. Mater. Rev.* **2012**, *57*, 357–382.

(11) Li, Y.; Fan, W.; Sun, H.; Cheng, X.; Li, P.; Zhao, X. Structural, electronic, and optical properties of α , β , and γ -TeO₂. *J. Appl. Phys.* **2010**, *107*, No. 093506.

(12) Boivin, G.; Bélanger, P.; Zednik, R. J. Characterization of Pure Face-Shear Strain in Piezoelectric α -Tellurium Dioxide (α -TeO₂). *Crystals* **2020**, *10*, 939.

(13) Mantsevich, S. N.; Kupreychik, M. I.; Balakshy, V. I. Possibilities of wide-angle tellurium dioxide acousto-optic cell application for the optical frequency comb generation. *Opt. Express* **2020**, *28*, 13243–13259.

(14) Itkin, V. P.; Alcock, C. B. The O-Te (Oxygen-Tellurium) System. *J. Phase Equilib.* **1996**, *17* (6), 533–538.

(15) Champarnaud-Mesjard, J. C.; Blanchandin, S.; Thomas, P.; Mirgorodsky, A.; Merle-Méjean, T.; Frit, B. Crystal structure, Raman spectrum and lattice dynamics of a new metastable form of tellurium dioxide: γ -TeO₂. *J. Phys. Chem. Solids* **2000**, *61*, 1499–1507.

(16) Ceriotti, M.; Pietrucci, F.; Bernasconi, M. Ab initio study of the vibrational properties of crystalline TeO₂: The α , β , and γ phases. *Phys. Rev. B* **2006**, *73*, No. 104304.

(17) Venimadhav, A. K. TeO₂: A Prospective High-k Dielectric. *Phys. Status Solidi* **2024**, *18*, No. 2300271.

(18) Moufok, S.; Kadi, L.; Amrani, B.; Khodja, K. D. Electronic structure and optical properties of TeO₂ polymorphs. *Results Phys.* **2019**, *13*, No. 102315.

(19) Naseri, M.; Jalilian, J.; Reshak, A. H. Electronic and optical properties of paratellurite TeO₂ under pressure: A first-principles calculation. *Optik* **2017**, *139*, 9–15.

(20) Dewan, N.; Sreenivas, K.; Gupta, V. Properties of crystalline γ -TeO₂ thin film. *J. Cryst. Growth* **2007**, *305*, 237–241.

(21) Roginskii, E. M.; Smirnov, M. B. Electronic Structure and Nonlinear Dielectric Susceptibility of γ -Phase of Tellurium Oxide. *Phys. Solid State* **2020**, *62*, 621–627.

(22) Zhang, H.; Swihart, M. T. Synthesis of Tellurium Dioxide Nanoparticles by Spray Pyrolysis. *Chem. Mater.* **2007**, *19*, 1290–1301.

(23) Arab, F.; Mousavi-Kamazani, M.; Salavati-Niasari, M. Facile sonochemical synthesis of tellurium and tellurium dioxide nanoparticles: Reducing Te(IV) to Te via ultrasonic irradiation in methanol. *Ultrason. Sonochem.* **2017**, *37*, 335–343.

(24) Arab, F.; Mousavi-Kamazani, M.; Salavati-Niasaria, M. Synthesis, characterization, and optical properties of Te, Te/TeO₂ and TeO₂ nanostructures via one-pot hydrothermal method. *RSC Adv.* **2016**, *6*, 71472–71480.

(25) Amari, A.; Al Mesfer, M. K.; Alsaiari, N. S.; Danish, M.; Alshahrani, A. M.; Tahoon, M. A.; Ben Rebah, F. Electrochemical and Optical Properties of Tellurium Dioxide (TeO₂) Nanoparticles. *Int. J. Electrochem. Sci.* **2021**, *16*, No. 210235.

(26) Cho, S. C.; Hong, Y. C.; Uhm, H. S. TeO₂ nanoparticles synthesized by evaporation of tellurium in atmospheric microwave-plasma torch-flame. *Chem. Phys. Lett.* **2006**, *429*, 214–218.

(27) El-Sayyad, G. S.; Mosallam, F. M.; El-Sayed, S. S.; El-Batal, A. I. Facile Biosynthesis of Tellurium Dioxide Nanoparticles by Streptomyces cyaneus Melanin Pigment and Gamma Radiation for Repressing Some Aspergillus Pathogens and Bacterial Wound Cultures. *J. Cluster Sci.* **2020**, *31*, 147–159.

(28) Qin, B.; Bai, Y.; Zhou, Y.; Liu, J.; Xie, X.; Zheng, W. Structure and characterization of TeO₂ nanoparticles prepared in acid medium. *Mater. Lett.* **2009**, *63*, 1949–1951.

(29) Khalef, W. K. Preparation and Characterization of TeO₂ Nanoparticles by Pulsed Laser Ablation in Water. *Eng. Technol. J.* **2014**, *32*, 396–405.

(30) Hesabizadeh, T.; Hicks, E.; Medina-Cruz, D.; Bourdo, S. E.; Watanabe, F.; Bonney, M.; Nichols, J.; Webster, T. J.; Guisbiers, G. Synthesis of “Naked” TeO₂ Nanoparticles for Biomedical Applications. *ACS Omega* **2022**, *7*, 23685–23694.

(31) Saraeva, I. N.; Tolordava, E. R.; Nastulyavichus, A. A.; Ivanova, A. K.; Kudryashov, S. I.; Rudenko, A. A.; Melnik, N. N.; Zayarny, D. A.; Ionin, A. A.; Romanova, Y. M.; Gonchukov, S. A. A bacterial

misericorde: laser-generated silicon nanorazors with embedded biotoxic nanoparticles combat the formation of durable biofilms. *Laser Phys. Lett.* **2020**, *17*, No. 025601.

(32) Khalef, W. K.; Marzoog, T. R.; Faisal, A. D. Synthesis and characterization of tellurium oxide nanoparticles using pulse laser ablation and study their antibacterial activity. *J. Phys.: Conf. Ser.* **2021**, *1795*, No. 012049.

(33) Guisbiers, G.; Mimun, L. C.; Mendoza-Cruz, R.; Nash, K. L. Synthesis of tunable tellurium nanoparticles. *Semicond. Sci. Technol.* **2017**, *32*, No. 04LT01.

(34) Liu, J.; Liang, C.; Zhu, X.; Lin, Y.; Zhang, H.; Wu, S. Understanding the Solvent Molecules Induced Spontaneous Growth of Uncapped Tellurium Nanoparticles. *Sci. Rep.* **2016**, *6*, No. 32631.

(35) Guisbiers, G.; Jose-Yacaman, M. Use of Chemical Functionalities to Control Stability of Nanoparticles. In *Encyclopedia of Interfacial Chemistry, Surface Science and Electrochemistry*; Elsevier, 2018; pp 875–885.

(36) Khairani, I. Y.; Mínguez-Vega, G.; Doñate-Buendía, C.; Gökce, B. Green nanoparticle synthesis at scale: a perspective on overcoming the limits of pulsed laser ablation in liquids for high-throughput production. *Phys. Chem. Chem. Phys.* **2023**, *25*, 19380–19408.

(37) Fazio, E.; Gökce, B.; De Giacomo, A.; Meneghetti, M.; Compagnini, G.; Tommasini, M.; Waag, F.; Lucotti, A.; Zanchi, C. G.; Ossi, P. M.; et al. Nanoparticles Engineering by Pulsed Laser Ablation in Liquids: Concepts and Applications. *Nanomaterials* **2020**, *10*, 2317.

(38) Amendola, V.; Amans, D.; Ishikawa, Y.; Koshizaki, N.; Scirè, S.; Compagnini, G.; Reichenberger, S.; Barcikowski, S. Room-Temperature Laser Synthesis in Liquid of Oxide, Metal-Oxide Core-Shells, and Doped Oxide Nanoparticles. *Chem. - Eur. J.* **2020**, *26*, 9206–9242.

(39) Whitmore Smith, A. John Tyndall (1820–1893). *Sci. Monthly* **1920**, *11*, 331–340.

(40) Ali, N.; Teixeira, J. A.; Addali, A. New pH Correlations for Stainless Steel 316L, Alumina, and Copper(I) Oxide Nanofluids Fabricated at Controlled Sonication Temperatures. *J. Nano Res.* **2019**, *58*, 125–138.

(41) Rodriguez, V.; Couzi, M.; Adamietz, F.; Dussauze, M.; Guery, G.; Cardinal, T.; Veber, P.; Richardson, K.; Thomas, P. Hyper-Raman and Raman scattering in paratellurite TeO₂. *J. Raman Spectrosc.* **2013**, *44*, 739–745.

(42) Guisbiers, G. Advances in thermodynamic modelling of nanoparticles. *Adv. Phys.: X* **2019**, *4*, No. 1668299.

(43) Roduner, E. Size matters: why nanomaterials are different. *Chem. Soc. Rev.* **2006**, *35*, 583–592.

(44) Geoffrion, L. D.; Guisbiers, G. Quantum confinement: size on the grill! *J. Phys. Chem. Solids* **2020**, *140*, No. 109320.